Transition Experiments on Blunt Bodies with Isolated Roughness Elements in Hypersonic Flight

D. C. Reda* and M. C. Wilder†

NASA Ames Research Center, Moffett Field, California 94035-1000

and

D. K. Prabhu‡

ELORET Corporation, Sunnyvale, California 94086-7607

Smooth titanium hemispheres with isolated three-dimensional surface-roughness elements were flown in the NASA Ames Research Center hypersonic ballistic range through quiescent CO_2 and air environments. Global surface intensity (temperature) distributions were optically measured and thermal wakes behind individual roughness elements were analyzed to define tripping effectiveness. Real-gas Navier–Stokes calculations of model flowfields, including laminar boundary-layer development in these flowfields, were conducted to predict key dimensionless parameters used to correlate transition on blunt bodies in hypersonic flow. For isolated roughness elements totally immersed within the laminar boundary layer, critical roughness Reynolds numbers for flights in air were found to be higher than those measured for flights in CO_2; i.e., it was easier to trip the CO_2 boundary layer to turbulence. Tripping effectiveness was found to be dependent on trip location within the subsonic region of the blunt-body flowfield, with effective tripping being most difficult to achieve for elements positioned closest to the stagnation point. Direct comparisons of critical roughness Reynolds numbers for three-dimensional isolated versus three-dimensional distributed roughness elements for flights in air showed that distributed roughness patterns were significantly more effective at tripping the blunt-body laminar boundary layer to turbulence.

Nomenclature

k	=	roughness height
M	=	Mach number
P	=	static pressure
Re_{kk}	=	roughness Reynolds number, $\rho_k u_k k / \mu_w$
Re_θ	=	momentum thickness Reynolds number, $\rho_e u_e \theta / \mu_e$
T	=	temperature
u	=	velocity
V_∞	=	model velocity at measurement station
δ	=	laminar boundary-layer thickness
θ	=	laminar boundary-layer momentum thickness
μ	=	fluid viscosity
ρ	=	fluid density
ϕ	=	azimuthal angle measured along hemisphere surface from stagnation point

Subscripts

e	=	at boundary-layer edge
k	=	at roughness height
stag	=	at stagnation point
TR	=	at transition
w	=	at wall conditions
∞	=	freestream

*Senior Research Scientist, Aerothermodynamics Branch, Mail Stop 230-2. Fellow AIAA.

†Aerospace Engineer, Aerothermodynamics Branch, Mail Stop 230-2. Associate Fellow AIAA.

‡Principal Research Scientist. Associate Fellow AIAA.

I. Introduction

MODELING of roughness-dominated transition to turbulence is an important design issue for ablating (single use) and nonablating (reusable) thermal protection systems (TPS). Two categories of surface roughness are associated with each type of TPS: distributed surface roughness and isolated surface roughness.

Ablating TPS, for single-use planetary-entry and Earth-return missions, first experience recession under high-altitude, low-Reynolds-number conditions. Such laminar-flow ablation causes the formation of a distributed surface microroughness pattern characteristic of the TPS material composition and fabrication process. Once formed, these distributed surface-roughness elements create disturbances within the laminar boundary layer flowing over the surface. As altitude decreases, Reynolds number increases, and flowfield conditions capable of amplifying these roughness-induced perturbations are eventually achieved, that is, transition onset occurs. Boundary-layer transition to turbulence results in more severe heat transfer rates and accelerated surface recession. Ablating TPS can thus potentially encounter failure mechanisms associated with exceeding bond-line temperature limits, burn through, or thermo-structural break up.

Ablating and nonablating TPS composed of many tiles or panels also have distributed surface-roughness patterns associated with the nominal (within design specifications) tile misalignments that inherently occur as the heat shield is assembled from discrete pieces. A classic example, for nonablating TPS, is found on the windward surface of the Space Shuttle *Orbiter*.

Distributed surface-roughness patterns generally cause transition to turbulence to occur simultaneously over large surface-area portions of the TPS, the boundary between the laminar-flow region and the turbulent-flow region being referred to as the transition front.

Isolated roughness elements, on the other hand, represent localized disturbance sources within the laminar boundary layer. Transition to turbulence behind any such discrete element occurs in a narrow, flow-aligned zone, its lateral extent usually spreading at shallow angles as the turbulent zone convects downstream.

Isolated roughness elements on ablating and reusable TPS are generally associated with design and/or assembly issues. Heat shields composed of discrete segments or tiles have two potential sources of isolated roughness elements: 1) localized tile surface

misalignments outside of design specifications and 2) the potential protrusion of gap-filler material placed between the tiles. Finally, all entry capsules are mated to launch vehicles, and a design feature must be employed to isolate the TPS material from launch accelerations and directly applied compressive loads. This can be accomplished by inserting compression pads of high-strength material at discrete locations within the TPS to allow for direct contact with adjacent load-bearing components. If these compression pads initially protrude above the TPS surface, or, due to differential ablation, protrude later in the entry trajectory, then the net result would be the formation of isolated surface-roughness elements.

Designers of ablating and nonablating TPS require physics-based criteria that allow for the accurate modeling of transition to turbulence as caused by either distributed roughness patterns or by isolated roughness elements.

The state of the art through 2002 concerning roughness-dominated transition to turbulence was summarized by Reda [1]. The primary conclusion of this review of published roughness-dominated transition correlations for blunt bodies, attachment lines and windward surfaces of lifting-entry vehicles was that all such correlations could be recast into, and be well modeled by, the critical roughness Reynolds number concept.

The concept of a critical roughness Reynolds number for transition is attributed to Schiller [2], who hypothesized that, at some critical value, vortices would be shed from the top of the roughness element (s), causing an abrupt breakdown to turbulence. The critical Reynolds number was based on smooth-wall laminar boundary-layer conditions at the roughness height, and the length scale was the roughness height. Citations given in [1] document the evolution of this concept from its inception up to 2002.

In 2004, Reshotko and Tumin [3] published the first-ever mathematical model for distributed-roughness-induced transition on blunt bodies in hypersonic flow. Their computational approach was based on spatial transient growth theory, pioneered by them, and predicted trends were found to be in general agreement with the critical roughness Reynolds number correlating approach. Comments on the databases used to calibrate their model were offered by Reda [4].

In 2006, Schneider [5] published a review article concerning transition on blunt reentry capsules and planetary probes. Issues related to the impact of transition on both TPS and afterbody flowfields were discussed. In this time frame, NASA interest was undergoing a dramatic shift away from lifting-entry vehicles, such as the Space Shuttle *Orbiter*, and was beginning to concentrate, once again, on blunt capsules such as the Crew Exploration Vehicle (CEV) for future manned missions.

Early 2008 saw the publication of a special issue of the *Journal of Spacecraft and Rocket*s dedicated, in large part, to transition on hypersonic vehicles. References [6–9], taken from this source, are most relevant to the present discussion.

In summary of the current state-of-the-art, the distributed-roughness-induced transition correlation of Reda et al. [8], based on quiescent, real-gas, hypersonic experiments conducted in ballistic ranges, offers a design tool for TPS surface-roughness requirements on blunt-body geometries. A similar design correlation for isolated surface-roughness elements has been put forward by Berry and Horvath [9]. Amar et al. [10], and Berger [11] expanded the available isolated-roughness database to include the CEV blunt-capsule geometry. However, the published wind-tunnel databases of [10,11] have yet to be analyzed within the critical roughness Reynolds number framework.

The objective of the present research was thus to acquire and analyze a new database for the influence of isolated roughness elements on blunt-body transition using quiescent, real-gas, ballistic-range testing methodologies [12].

II. Experimental Approach

The experiments were performed in the Hypervelocity Free Flight Aerodynamic Facility, part of the ballistic-range complex at NASA Ames Research Center. The ballistic range, shown in Fig. 1, employs a two-stage light-gas gun to launch individual models on trajectories through a controlled-atmosphere test section. The largest gun has an inner diameter of 38.1 mm (1.5 in.), and the test section is approximately 1 m across and 23 m long, measured from the first optical measurement station to the last. The models are in flight for an additional 10 m from the exit of the gun barrel to the first optical measurement station, during which time the launch sabot is separated from the model and trapped in the receiver tank. There are 16 optical measurement stations, spaced 1.524 m (5 ft) apart, along the length of the test section. Each station is equipped with orthogonal-viewing parallel-light shadowgraph cameras and high-speed timers for recording the flight trajectories. Figure 2 shows a shadowgraph picture of a model in hypersonic free flight. Pitch and yaw angles
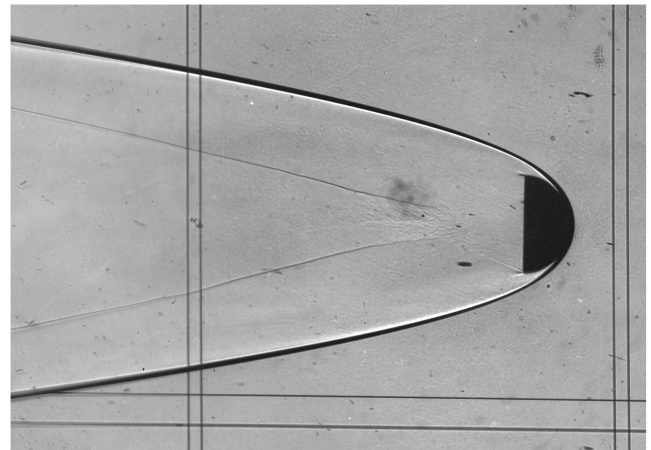

Fig. 2 Shadowgraph of model in hypersonic free flight in CO_2, $V_\infty = 4$ km/s, $P_\infty = 0.2$ atm.
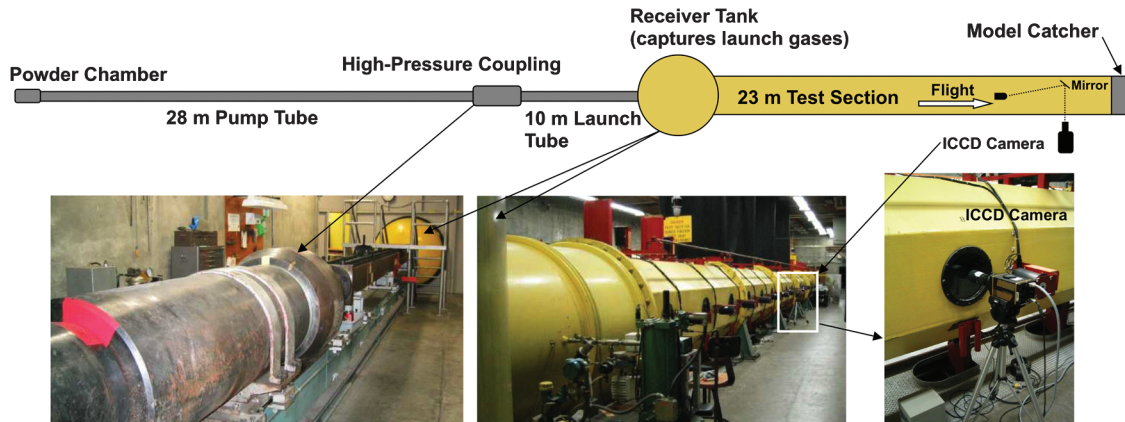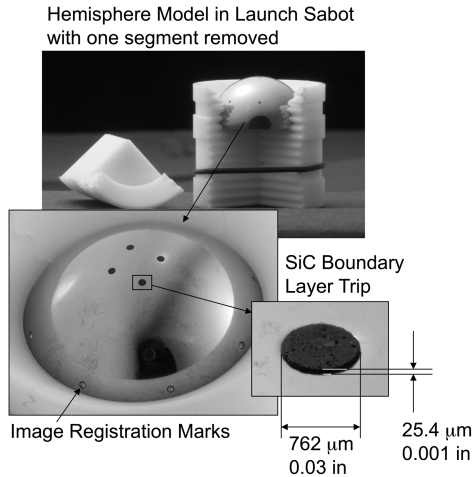

**Fig. 1 The NASA Ames Research Center free-flight ballistic range.**

Fig. 3 Titanium hemisphere model with SiC boundary-layer trips located 10 deg from the stagnation point, shown in launch sabot with one segment removed.

were measured from orthogonal-view photographs taken at multiple stations along each range trajectory and were generally less than a few degrees.

Figure 3 shows a photograph of a hemispherical model, and its launch sabot, used in the present experiments. The hemispheres were made from commercially available titanium alloy (Ti-6Al-4V) ball bearings with a diameter of 2.86 cm (1.125 in.), which were cut in half using an electrical discharge machining wire. The arithmetical average surface roughness of these polished spheres was 0.2 μm (grade-200 balls, as defined by the Anti Friction Bearing Manufacturers Association standards), giving an aerodynamically smooth surface finish. Transition was never observed on the polished model surface, only downstream of isolated roughness elements.

Isolated disklike surface-roughness elements were created by drilling holes perpendicular to the model surface at parametrically varied locations of 10, 20, and 30° of arc length from the stagnation point, then press-fitting cylindrical silicon carbide pins of diameter 762 μm (0.030 in.) into each hole, leaving exposed heights that were systematically varied to cover a wide range of Re_{kk} values. Four such pins were located on each model, all at the same arc length from the stagnation point, and always separated by 90° circumferentially.
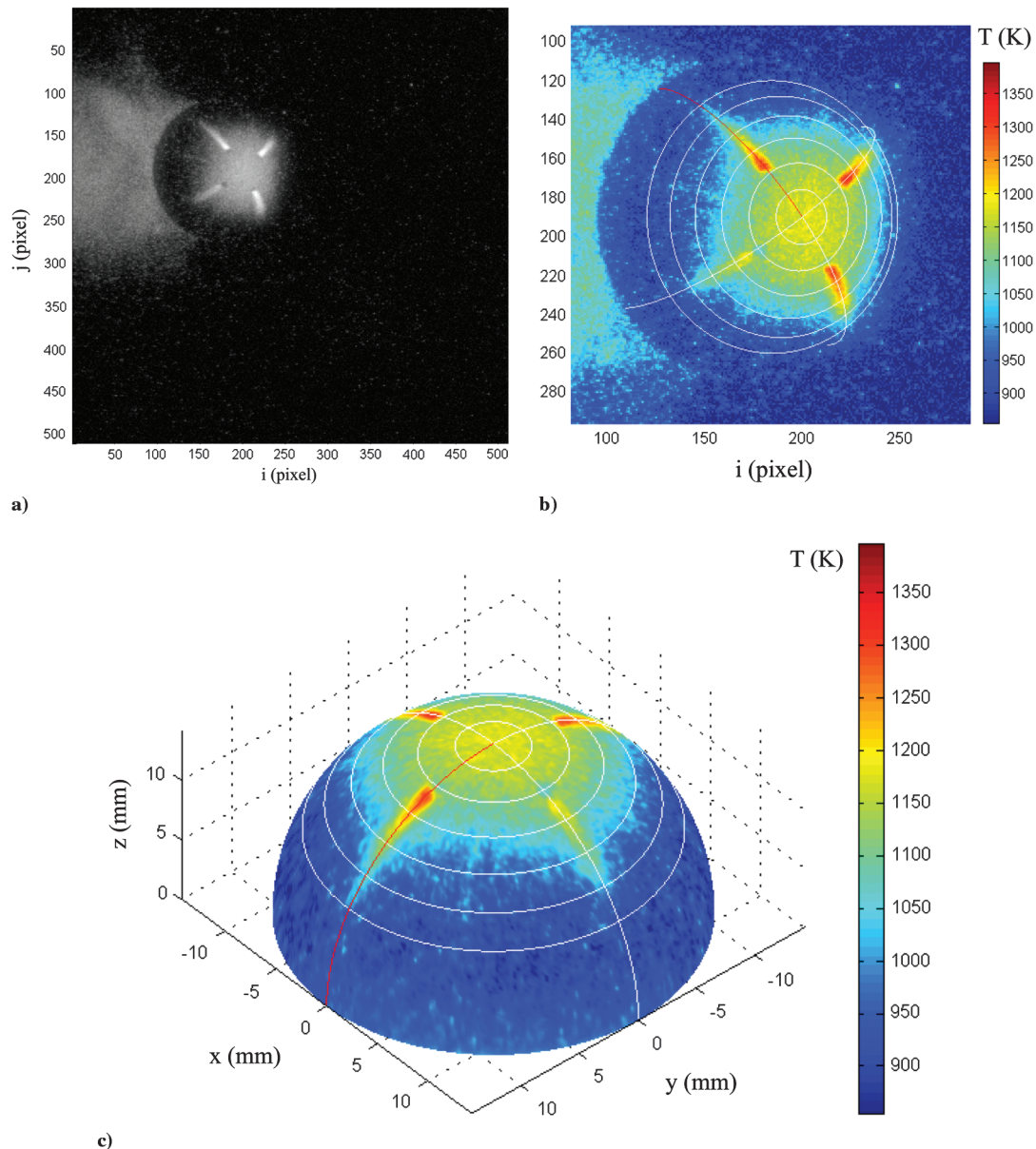
Fig. 4 Example thermal image of hemisphere in flight through CO_2, $V_\infty = 4.0$ km/s, $P_\infty = 0.2$ atm, with trips at $\phi = 20°$: a) global surface intensity distribution, b) global surface temperature distribution with coordinate grid mapping, and c) temperature image after resection to 3-D coordinate grid.
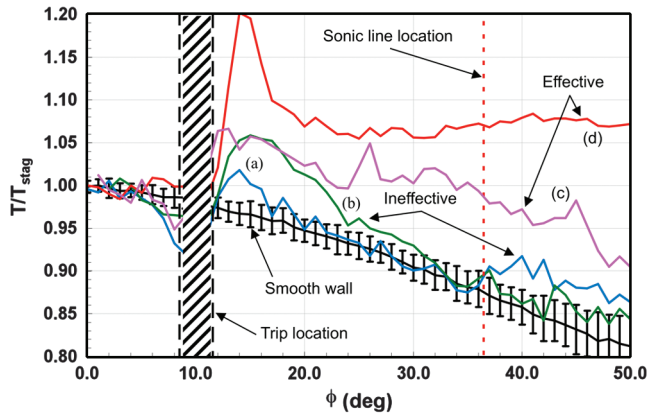
Fig. 5 Examples of measured surface temperature profiles along roughness element wake centerlines for tests in CO_2: a) $k/\delta = 0.6$, $Re_{kk} = 603$, and $P_\infty = 0.2$ atm; b) $k/\delta = 0.78$, $Re_{kk} = 779$, and $P_\infty = 0.2$ atm; c) $k/\delta = 0.78$, $Re_{kk} = 779$, and $P_\infty = 0.2$ atm; and d) $k/\delta = 0.82$, $Re_{kk} = 982$, and $P_\infty = 0.3$ atm.

Fig. 7 Summary of effective-tripping limits for CO_2.

Roughness element heights, which ranged from 0.0002 to 0.002 in., were measured using greatly magnified silhouette images generated with an optical comparator.

For these experiments, six of the optical measurement stations were equipped with high-speed thermal imaging cameras to record the instantaneous global surface intensity distributions on the models. Three stations employed intensified charge-coupled-device (ICCD) cameras sensitive to the visible wavelengths of light, and three employed infrared cameras sensitive to the 3–5 μm infrared band. The cameras were located outside the test section and viewed the models off a first-surface plane mirror placed inside the test section, just off the line of flight, as illustrated schematically in Fig. 1. An example ICCD image is shown in Fig. 4a. The luminous wake of the model can be seen in this image. The shock-layer gases of the bow shock also radiate intensely in the visible wavelengths for the conditions of these experiments and have the potential to bias the surface temperature measurements. A localized plume of helium was created to temporarily quench this gas-cap radiation at each ICCD imaging station, as discussed in [12]. The model was in the helium less than 0.5% of the total flight time; thus, its effect on the integrated convective heating over the entire trajectory was minimal. There is no appreciable gas-cap radiation in a narrowband around 4 μm. A notch
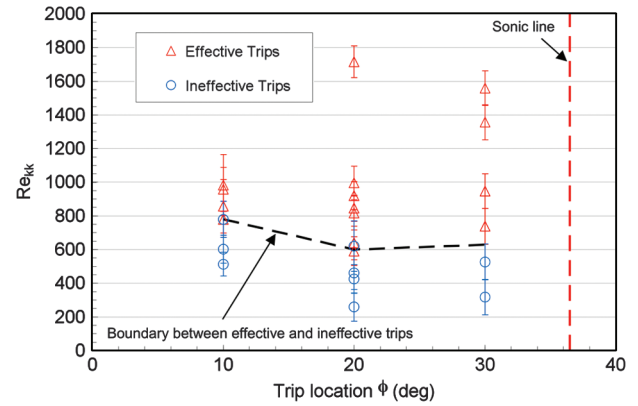
filter at 4 μm $\pm$ 0.15 μm was used with the midwave infrared waveband, so no helium plume was required for those cameras. Only the data obtained with the ICCD cameras are reported here.

Camera calibration procedures outlined in [12,13] were employed to convert intensity images to global surface temperature images (see Fig. 4b) and, finally, to 3-D surface temperature maps, as shown in Fig. 4c. The response of each camera was calibrated against a National Institute of Standards and Technology (NIST)-traceable blackbody standard by imaging the blackbody source on an optical path equivalent to that employed in the ballistic-range tests. For typical camera parameters used (intensifier gain and lens aperture), the standard deviation of temperature measurements for temperatures above 900 K was $\pm$6 K, both for pixel-to-pixel variations within an image of a uniform source and for image-to-image variations for a given pixel. Camera parameters were adjusted so that the peak expected temperature for a shot condition would result in as intense an image as possible without saturating the sensors. As a result, the minimum detectable temperature was typically around 950 K with the ICCD cameras. All images were recorded with a 0.5 μs exposure time.

Both air and CO_2 were employed as test gases. Freestream pressure levels were varied from 0.15 to 0.35 atm, and freestream temperature of the quiescent test gas was at room temperature ranging from 292 to 298 K. Model/sabot packages were launched from a two-stage light-gas gun at a nominal muzzle velocity of 4.5 km/s, yielding freestream velocities on the order of 4 km/s at
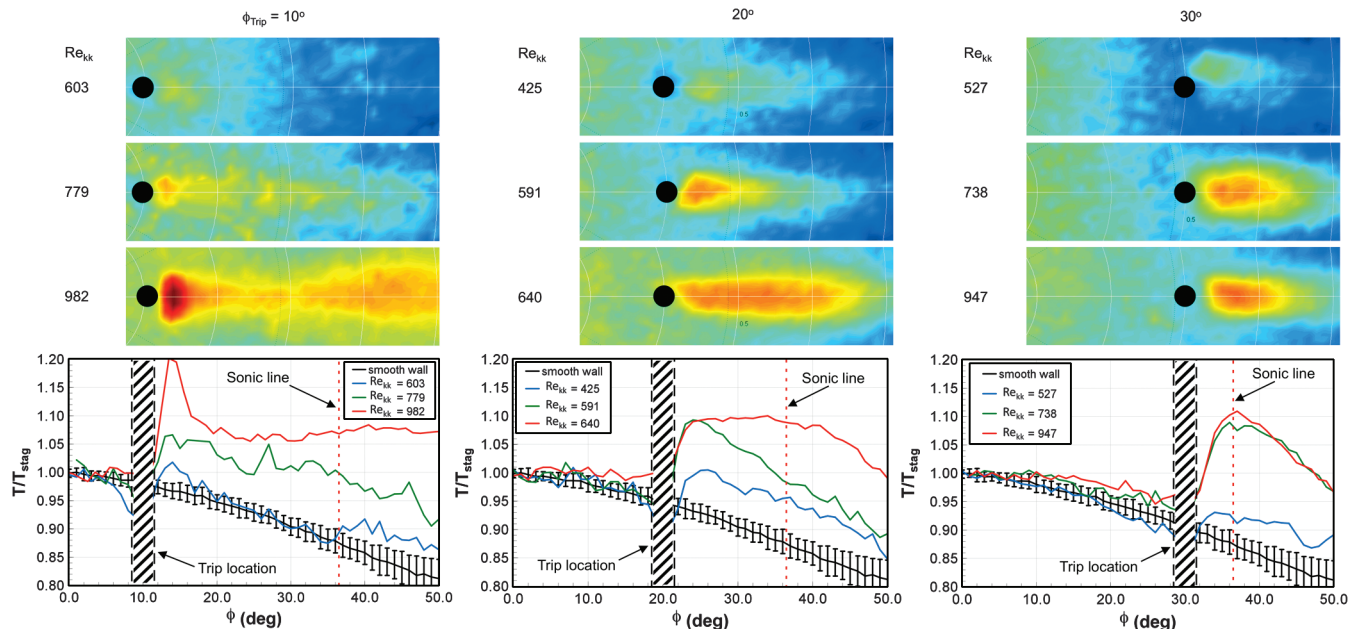

Fig. 6 Selected thermal wakes and wake centerline profiles for trips at $\phi = 10$, 20, and 30 deg for experiments in CO_2.

Table 1   Summary of data for experiments in CO_2

P_∞, atm	V_∞, km/s	$Re_\theta{}^a$	M_e	k, μm	k, in	k/δ	Re_{kk}	Effective?
			$\phi_{Trip} = 10.0$ deg					
0.20	3.91	67.4	0.27	15	0.0006	0.52	514	No
0.20	3.92	67.5	0.27	18	0.0007	0.60	603	No
0.20	3.91	67.4	0.27	23	0.0009	0.78	779	No
0.20	3.92	67.5	0.27	23	0.0009	0.78	779	Yes
0.20	3.91	67.4	0.27	23	0.0009	0.78	779	Yes
0.30	3.67	80.6	0.26	18	0.0007	0.72	858	Yes
0.30	3.67	80.6	0.26	18	0.0007	0.72	858	Yes
0.30	3.67	80.6	0.26	20	0.0008	0.82	982	Yes
0.20	3.91	67.4	0.27	28	0.0011	0.95	958	Yes
			$\phi_{Trip} = 20.0$ deg					
0.200	3.91	129.3	0.53	5	0.0002	0.16	260	No
0.200	4.01	129.3	0.53	8	0.0003	0.24	425	No
0.219	4.00	134.2	0.53	8	0.0003	0.25	462	No
0.175	3.94	122.9	0.54	10	0.0004	0.34	621	No
0.200	4.01	129.3	0.53	10	0.0004	0.32	591	Yes
0.200	4.01	129.3	0.53	10	0.0004	0.32	591	Yes
0.219	4.00	134.2	0.53	10	0.0004	0.33	640	Yes
0.219	4.00	134.2	0.53	13	0.0005	0.42	817	Yes
0.175	3.94	122.9	0.54	15	0.0006	0.46	846	Yes
0.175	3.94	122.9	0.54	15	0.0006	0.46	846	Yes
0.175	3.94	122.9	0.54	15	0.0006	0.46	846	Yes
0.200	3.91	129.3	0.53	15	0.0006	0.49	920	Yes
0.200	4.01	129.3	0.53	15	0.0006	0.49	920	Yes
0.219	4.00	134.2	0.53	15	0.0006	0.50	996	Yes
0.200	3.94	129.3	0.53	28	0.0011	0.89	1715	Yes
0.200	3.94	129.3	0.53	28	0.0011	0.89	1715	Yes
			$\phi_{Trip} = 30.0$ deg					
0.20	4.10	183.1	0.81	5	0.0002	0.14	317	No
0.20	4.05	182.8	0.81	8	0.0003	0.22	527	No
0.20	4.10	183.1	0.81	10	0.0004	0.29	738	Yes
0.20	4.10	183.1	0.81	10	0.0004	0.29	738	Yes
0.20	4.05	182.8	0.81	10	0.0004	0.29	738	Yes
0.20	4.05	182.8	0.81	10	0.0004	0.29	738	Yes
0.20	3.92	182.9	0.81	13	0.0005	0.36	947	Yes
0.20	4.10	183.1	0.81	13	0.0005	0.36	947	Yes
0.20	4.05	182.8	0.81	13	0.0005	0.36	947	Yes
0.20	3.92	182.9	0.81	18	0.0007	0.50	1357	Yes
0.20	3.92	182.9	0.81	20	0.0008	0.58	1559	Yes
0.20	3.92	182.9	0.81	28	0.0011	0.79	2157	Yes

[a]Corrected values versus those reported in [17].

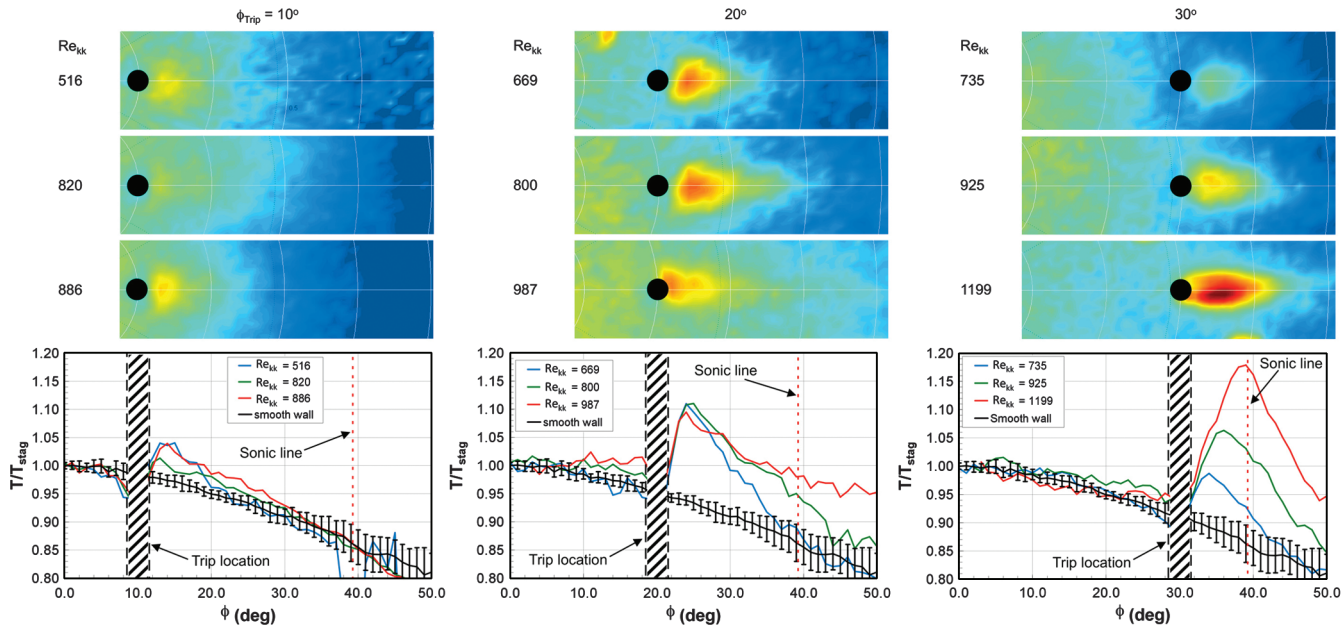

Fig. 8   Selected thermal wakes and wake centerline profiles for trips at $\phi = 10$, 20, and 30 deg for experiments in air.
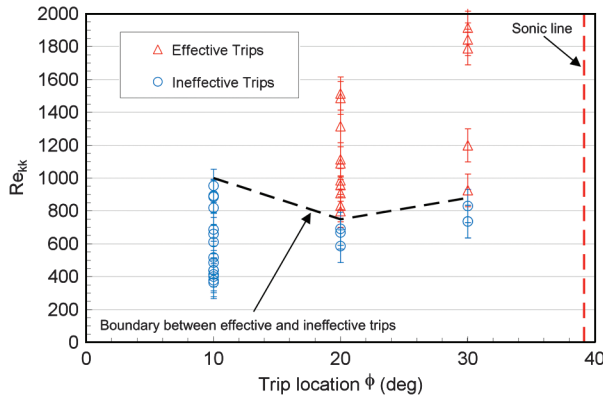
Fig. 9   Summary of effective-tripping limits for air.

midrange locations. Corresponding nominal freestream Mach numbers were 12 for air and 15 for CO_2. The majority of the experiments were performed at a freestream pressure level of 0.2 atm.

Laminar boundary-layer development around the hemispherical model was computed for each test case using the data-parallel line-relaxation code [14] (see discussions in [8]). The coefficients of viscosity and thermal conductivity for the reacting gas mixture in the shock layer are computed using the latest collision integral data [15,16] for all relevant species pairs. Results of these real-gas Navier–Stokes calculations were combined with measured trip heights and trip locations to define roughness Reynolds numbers (Re_{kk} values), which ranged from order 200 to order 2000 in the present experiments. The ratio of roughness height k to boundary-layer thickness δ was always set to be less than one. The critical roughness Reynolds number value for distributed roughness on a hemispherical body for hypersonic flight through air is $Re_{kk,\mathrm{TR}} = 250$ [8].

Table 2   Summary of data for experiments in air

P_∞, atm	V_∞, km/s	$Re_\theta{}^{\mathrm{a}}$	M_e	k, μm	k, in	k/δ	Re_{kk}	Effective?
			$\phi_{\mathrm{Trip}} = 10.0$ deg					
0.171	4.13	39.7	0.25	25	0.0010	0.49	366	No
0.180	4.10	40.6	0.25	25	0.0010	0.50	378	No
0.171	4.13	39.7	0.25	28	0.0011	0.54	401	No
0.180	4.10	40.6	0.25	28	0.0011	0.55	414	No
0.180	4.10	40.6	0.25	28	0.0011	0.55	414	No
0.199	4.00	42.5	0.25	28	0.0011	0.57	439	No
0.199	4.00	42.5	0.25	28	0.0011	0.57	439	No
0.199	4.00	42.5	0.25	28	0.0011	0.57	439	No
0.180	4.10	40.6	0.25	33	0.0013	0.65	486	No
0.199	4.00	42.5	0.25	33	0.0013	0.68	516	No
0.171	4.13	39.7	0.25	43	0.0017	0.83	611	No
0.150	4.29	37.7	0.25	51	0.0020	0.92	660	No
0.350	3.98	57.2	0.24	25	0.0010	0.64	686	No
0.350	3.98	57.2	0.24	30	0.0012	0.76	819	No
0.350	3.98	57.2	0.24	33	0.0013	0.83	886	No
0.350	3.98	57.2	0.24	33	0.0013	0.83	886	No
0.305	3.99	52.8	0.24	38	0.0015	0.90	894	No
0.305	3.99	52.8	0.24	41	0.0016	0.95	953	No
			$\phi_{\mathrm{Trip}} = 20.0$ deg					
0.175	4.09	77.3	0.50	25	0.0010	0.46	669	No
0.185	4.03	79.2	0.49	25	0.0010	0.47	691	No
0.175	4.09	77.3	0.50	30	0.0012	0.55	800	Yes
0.211	4.06	84.0	0.49	28	0.0011	0.54	833	Yes
0.211	4.06	84.0	0.49	28	0.0011	0.54	833	Yes
0.211	4.06	84.0	0.49	30	0.0012	0.59	907	Yes
0.211	4.06	84.0	0.49	30	0.0012	0.59	907	Yes
0.185	4.03	79.2	0.49	36	0.0014	0.66	958	Yes
0.185	4.03	79.2	0.49	36	0.0014	0.66	958	Yes
0.350	3.81	110.7	0.49	20	0.0008	0.44	987	Yes
0.185	4.03	79.2	0.49	41	0.0016	0.76	1090	Yes
0.350	3.81	110.7	0.49	23	0.0009	0.49	1114	Yes
0.175	4.09	77.3	0.50	51	0.0020	0.92	1314	Yes
0.350	3.81	110.7	0.49	30	0.0012	0.66	1488	Yes
0.175	4.09	77.3	0.50	58	0.0023	1.06	1514	Yes
			$\phi_{\mathrm{Trip}} = 30.0$ deg					
0.200	4.13	117.6	0.75	20	0.0008	0.35	735	No
0.200	4.22	117.6	0.75	20	0.0008	0.35	735	No
0.200	4.22	117.6	0.75	20	0.0008	0.35	735	No
0.200	4.22	117.6	0.75	23	0.0009	0.40	830	No
0.200	4.22	117.6	0.75	25	0.0010	0.44	925	Yes
0.200	4.13	117.6	0.75	25	0.0010	0.44	925	Yes
0.201	4.08	117.7	0.75	33	0.0013	0.57	1199	Yes
0.201	4.08	117.7	0.75	33	0.0013	0.57	1199	Yes
0.250	4.01	131.4	0.74	33	0.0013	0.61	1789	Yes
0.250	4.01	131.4	0.74	33	0.0013	0.61	1789	Yes
0.300	3.90	145.0	0.74	28	0.0011	0.56	1844	Yes
0.201	4.08	117.7	0.75	53	0.0021	0.93	1915	Yes
0.300	3.90	145.0	0.74	30	0.0012	0.61	2007	Yes
0.300	3.90	145.0	0.74	30	0.0012	0.61	2007	Yes
0.300	3.90	145.0	0.74	33	0.0013	0.66	2170	Yes
0.250	4.01	131.4	0.74	51	0.0020	0.94	2733	Yes

$^{\mathrm{a}}$Corrected values versus those reported in [17].

III. Effective-Tripping (Transition) Criterion

It was required that a single consistent criterion be identified and applied to each trip in each experiment in order to define whether or not an individual isolated roughness element was effective at tripping the laminar boundary layer to turbulence. The basic measurement in all these experiments was the global surface temperature distribution; hence, the tripping effectiveness criterion was based on these recorded observations (see Fig. 5). Data are presented in a nondimensional form, using the measured stagnation point temperature for each shot to normalize shot-to-shot differences in freestream pressure and velocity.

Each surface temperature distribution measured along a roughness element wake centerline was compared to a composite of undisturbed laminar streamwise distributions measured at circumferential angles taken between pin locations on the smooth-wall segments of the hemisphere. The smooth-wall nondimensional profiles shown in Fig. 5 and subsequent figures are profiles averaged over many shots. The error bars represent the root sum square of the standard deviation of the mean profile and the calibration uncertainty of ±6 K. Error bars are not shown on the trip wake profiles to avoid clutter, but are of similar magnitude. At low Re_{kk} values, surface temperature perturbations behind the trip were minimal, quickly returning to laminar levels (see curve a in Fig. 5); at intermediate Re_{kk} values (curve b in Fig. 5), an abrupt surface temperature rise was seen in the trip near-wake region, but this disturbance also decayed back to the local undisturbed laminar level as the mean flow expanded around the hemispherical model; at higher Re_{kk} values, an abrupt surface temperature rise in the trip near-wake region was also seen, but in such effective-tripping cases, surface temperature levels remained above the composite laminar curve to well beyond the sonic line location (see range of responses indicated by curves c and d in Fig. 5).

Wakes of such effective isolated roughness elements are clearly turbulent in nature, although the wake may not produce heat transfer rates equivalent to those of a fully developed turbulent flow. Comparisons with predicted turbulent heat fluxes (or surface temperatures) were not employed in the present study so as to avoid issues concerning the validity of available turbulence models.

In certain testing applications, a spanwise array of isolated roughness elements is sometimes used to trip the approaching laminar boundary layer to a fully developed turbulent state. Such a response is generally not achieved until wakes of the individual roughness elements merge at some finite distance downstream of the trip array [10,11] and may depend on other factors, such as freestream Reynolds number.

IV. Effective-Tripping Results

A. CO_2 Data

Figure 6 shows a composite of selected trip thermal wakes and wake centerline axial cuts taken from the CO_2 experiments. Parametric values of trip angular location are listed at the top of each column. The roughness Reynolds number value is listed at the left-hand edge of each image, and the magnitude of this critical parameter increases, top to bottom, as listed in each column. As can be seen for each trip location, systematic increases in the roughness Reynolds number resulted in stronger and more enduring thermal perturbations in the roughness element wake. Employing the tripping effectiveness criterion outlined in Fig. 5, the critical value of $Re_{kk,TR}$ could be determined at each angular trip location by noting the transition from ineffective to effective tripping, depicted here by the dashed line separating the two regimes (see Fig. 7 and Table 1; Re_θ values have been corrected versus those reported in [17]). Critical roughness Reynolds numbers for an isolated roughness element on a blunt body at hypersonic speeds in CO_2 were thus found (for $10° \le \phi \le 30°$) to be in the range $\sim 600 \le Re_{kk,TR} \le \sim 800$, where $k/\delta < 1$.

Maximum resistance to input disturbances (highest $Re_{kk,TR}$ value) occurred at the upstream-most location ($\phi = 10°$), where the local edge Mach number and momentum thickness Reynolds number were low.
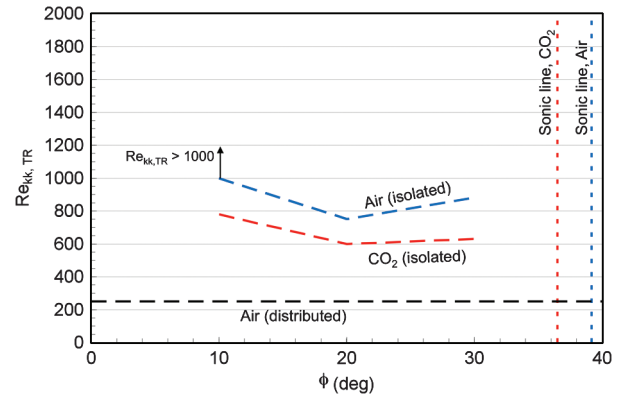

Fig. 10   Critical Re_{kk} values for isolated and distributed roughness elements on blunt (hemispherical) bodies in hypersonic free flight.

B. Air Data

Figure 8 shows a composite of selected trip thermal wakes and wake centerline axial cuts taken from the air experiments, using the same format as employed in Fig. 6. For trips located at $\phi = 20$ and $30°$, systematic increases in the roughness Reynolds number resulted in large thermal perturbations in these trip wakes, both in magnitude and in physical extent, consistent with the attainment of effective tripping to turbulence.

Important differences, however, between the air and CO_2 results were noted (compare the $\phi = 10°$ images between Figs. 6 and 8). Subject to the limiting conditions $k/\delta < 1$ and $P_\infty < 0.375$ atm (to avoid ignition of the titanium model), maximum attainable Re_{kk} values at $10°$ in air were on the order of 1000, a value insufficient to cause an effective breakdown to turbulence at this location.

Figure 9 and Table 2 summarize the ineffective versus effective-tripping results for isolated roughness elements on blunt bodies in hypersonic flight through air as a function of trip location. Re_θ values in Table 2 have been corrected versus those reported in [17]. The dashed line separating these two regimes yielded $\sim 750 \le Re_{kk,TR} \le \sim 850$ for $20° \le \phi \le 30°$, $k/\delta < 1$.

The line separating these two regimes was extended to $Re_{kk} = 1000$ at $\phi = 10°$ as an estimate only.

V. Comparison of CO_2 and Air Results

Figure 10 summarizes current and published data bases for the tripping effectiveness of isolated and distributed roughness elements on blunt (hemispherical) bodies in hypersonic free flight. Two principal observations present themselves. First, for isolated roughness elements, it is easier to trip the laminar boundary layer to turbulence for trajectories flown in CO_2 versus air, a finding that has consequences for Mars entry missions. Second, as noted earlier in the review paper of [8], distributed roughness patterns are much more efficient at tripping laminar boundary layers to turbulence than isolated roughness elements. For blunt bodies at hypersonic speeds in air,

$$\frac{Re_{kk,TR}(\text{isolated})}{Re_{kk,TR}(\text{distributed})} \cong \frac{800}{250} \cong \frac{3}{1}$$

VI. Conclusions

1) Critical roughness Reynolds number was found to correlate effective-tripping results for isolated roughness elements immersed within the laminar boundary layer and positioned within the subsonic region of blunt bodies in hypersonic free flight.

2) Critical roughness Reynolds numbers for such isolated roughness elements were found to be higher for flights in air versus CO_2 by ratios of $\sim 1.3/1$; i.e., for a specified isolated roughness element, it was easier to trip the CO_2 boundary layer to turbulence.

3) For both CO_2 and air, tripping effectiveness of such isolated roughness elements showed a dependence on location within the subsonic region; tripping was most difficult to achieve for elements positioned closest to the stagnation point.

4) Present air results, compared to transition data for distributed roughness patterns on blunt bodies in hypersonic free flight, showed that distributed roughness patterns are significantly more effective at causing transition to turbulence. Specifically, critical roughness Reynolds numbers for isolated roughness elements were on the order of three times larger than corresponding values for distributed roughness patterns.

Acknowledgments

References

[1] Reda, D. C., "Review and Synthesis of Roughness-Dominated Transition Correlations for Reentry Applications," *Journal of Spacecraft and Rockets*, Vol. 39, No. 2, March–April 2002, pp. 161–167.
doi:10.2514/2.3803

[2] Schiller, L., "Flow in Pipes," *Handbook of Experimental Physics*, Vol. 4, Pt. 4, Academic Press, Leipzig, Germany, 1932, pp. 189–192.

[3] Reshotko, E., and Tumin, A., "Role of Transient Growth in Roughness-Induced Transition," *AIAA Journal*, Vol. 42, No. 4, April 2004, pp. 766–770.
doi:10.2514/1.9558

[4] Reda, D. C., "Comment on 'Role of Transient Growth in Roughness-Induced Transition'," *AIAA Journal*, Vol. 42, No. 4, April 2004, p. 771.
doi:10.2514/1.3706

[5] Schneider, S. P., "Laminar-Turbulent Transition on Reentry Capsules and Planetary Probes," *Journal of Spacecraft and Rockets*, Vol. 43, No. 6, Nov.–Dec. 2006, pp. 1153–1173.
doi:10.2514/1.22594

[6] Reshotko, E., "Transition Issues for Atmospheric Entry," *Journal of Spacecraft and Rockets*, Vol. 45, No. 2, March–April 2008, pp. 161–164.
doi:10.2514/1.29777

[7] Schneider, S. P., "Effects of Roughness on Hypersonic Boundary-Layer Transition," *Journal of Spacecraft and Rockets*, Vol. 45, No. 2, March–April 2008, pp. 193–209.
doi:10.2514/1.29713

[8] Reda, D. C., Wilder, M. C., Bogdanoff, D. W., and Prabhu, D. K., "Transition Experiments on Blunt Bodies with Distributed Roughness in Hypersonic Free Flight," *Journal of Spacecraft and Rockets*, Vol. 45, No. 2, March–April 2008, pp. 210–215.
doi:10.2514/1.30288

[9] Berry, S. A., and Horvath, T. J., "Discrete-Roughness Transition for Hypersonic Flight Vehicles," *Journal of Spacecraft and Rockets*, Vol. 45, No. 2, March–April 2008, pp. 216–227.
doi:10.2514/1.30970

[10] Amar, A. J., Horvath, T. J., Hollis, B. R., Berger, K. T., Berry, S. A., and Calvert, N., "Protuberance Boundary Layer Transition for Project Orion Crew Entry Vehicle," 46th Aerospace Sciences Meeting, AIAA Paper 2008-1227, Reno, NV, Jan. 2008.

[11] Berger, K. T., "Aerothermodynamic Testing of the Crew Exploration Vehicle in the LaRC 20-Inch Mach 6 and 31-Inch Mach 10 Tunnels," *46th Aerospace Sciences Meeting*, AIAA Paper 2008-1225, Reno, NV, Jan. 2008.

[12] Reda, D. C., Wilder, M. C., Bogdanoff, D. W., and Olejniczak, J., "Aerothermodynamic Testing of Ablative Reentry Vehicle Nosetip Materials in Hypersonic Ballistic-Range Environments," *1st U.S. Air Force Developmental Test and Evaluation (DT&E) Summit*, AIAA Paper 2004-6829, Woodland Hills, CA, Nov. 2004.

[13] Wilder, M. C., Reda, D. C., Bogdanoff, D. W., and Prabhu, D. K., "Free-Flight Measurements of Convective Heat Transfer in Hypersonic Ballistic-Range Environments," 39th AIAA Thermophysics Conference, AIAA Paper 2007-4404, Miami, FL, June 25–28, 2007.

[14] Wright, M. J., Candler, G. V., and Bose, D., "Data-Parallel Line Relaxation Method for the Navier–Stokes Equations," *AIAA Journal*, Vol. 36, No. 9, 1998, pp. 1603–1609.
doi:10.2514/2.586

[15] Wright, M. J., Bose, D. K., Palmer, G. E., and Levin, E., "Recommended Collision Integrals for Transport Property Computations Part 1: Air Species," *AIAA Journal*, Vol. 43, No. 12, 2005, pp. 2558–2564.
doi:10.2514/1.16713

[16] Wright, M. J., Hwang, H. H., and Schwenke, D., "Recommended Collision Integrals for Transport Property Computations Part II: Mars and Venus Entries," *AIAA Journal*, Vol. 45, No. 1, 2007, pp. 281–288.
doi:10.2514/1.24523

[17] Reda, D. C., Wilder, M. C., and Prabhu, D. K., "Transition Experiments on Blunt Bodies with Isolated Roughness Elements in Hypersonic Free Flight," 48th Aerospace Sciences Meeting, AIAA Paper 2010-1367, Orlando, FL, Jan. 2010.

R. Kimmel
Associate Editor